

Submolecular Ligand Size and Spacing for Cell Adhesion

Yuri Kim, Thomas Myeongseok Koo, Ramar Thangam, Myeong Soo Kim, Woo Young Jang, Nayeon Kang, Sunhong Min, Seong Yeol Kim, Letao Yang, Hyunsik Hong, Hee Joon Jung, Eui Kwan Koh, Kapil D. Patel, Sungkyu Lee, Hong En Fu, Yoo Sang Jeon, Bum Chul Park, Soo Young Kim, Steve Park, Junmin Lee, Luo Gu, Dong-Hyun Kim, Tae-Hyung Kim, Ki-Bum Lee, Woong Kyo Jeong, Ramasamy Paulmurugan,* Young Keun Kim,* and Heemin Kang*

Cell adhesion occurs when integrin recognizes and binds to Arg–Gly–Asp (RGD) ligands present in fibronectin. In this work, submolecular ligand size and spacing are tuned via template-mediated in situ growth of nanoparticles for dynamic macrophage modulation. To tune liganded gold nanoparticle (GNP) size and spacing from 3 to 20 nm, in situ localized assemblies of GNP arrays on nanomagnetite templates are engineered. 3 nm-spaced ligands stimulate the binding of integrin, which mediates macrophage-adhesion-assisted pro-regenerative polarization as compared to 20 nm-spaced ligands, which can be dynamically anchored to the substrate for stabilizing integrin binding and facilitating dynamic macrophage adhesion. Increasing the ligand size from 7 to 20 nm only slightly promotes macrophage adhesion, not observed with 13 nm-sized ligands. Increasing the ligand spacing from 3 to 17 nm significantly hinders macrophage adhesion that induces inflammatory polarization. Submolecular tuning of ligand spacing can dominantly modulate host macrophages.

1. Introduction

In natural tissue, the extracellular matrix (ECM) is organized by cell-adhesive ECM proteins such as fibronectin (FN), laminin, and collagen, which determine the heterogeneous structure of the ECM and continuously regulates the recruitment, adhesion formation, and subsequent functionality of immunomodulatory host cells^[1–3] such as macrophages.^[4–10] For instance, heterogeneously distributed FN in the ECM structure^[11] functionally modulates the migration,^[12] phagocytosis,^[13] ECM production,^[14] and inflammatory M1 versus anti-inflammatory/pro-healing M2 polarization of macrophages,^[15–17] which regulate inflammation, wound healing,

Y. Kim, T. M. Koo, R. Thangam, N. Kang, S. Min, S. Y. Kim, H. Hong, K. D. Patel, S. Lee, H. E. Fu, B. C. Park, S. Y. Kim, Y. K. Kim, H. Kang
Department of Materials Science and Engineering
Korea University

Seoul 02841, Republic of Korea
E-mail: ykim97@korea.ac.kr; heeminkang@korea.ac.kr

R. Thangam, M. S. Kim, K. D. Patel, S. Y. Kim
Institute for High Technology Materials and Devices
Korea University
Seoul 02841, Republic of Korea

W. Y. Jang, W. K. Jeong
Department of Orthopedic Surgery
Korea University Anam Hospital
Seoul 02841, Republic of Korea

L. Yang, K.-B. Lee
Department of Chemistry and Chemical Biology
Rutgers University
Piscataway, NJ 08854, USA

H. J. Jung
Department of Materials Science and Engineering
Northwestern University
Evanston, IL 60208, USA

H. J. Jung
International Institute for Nanotechnology
Evanston, IL 60208, USA

H. J. Jung
NUANCE Center
Northwestern University
Evanston, IL 60208, USA


E. K. Koh
Seoul Center
Korea Basic Science Institute
145 Anam-Ro, Seongbuk-Gu, Seoul 02841, Republic of Korea

Y. S. Jeon
Institute of Engineering Research
Korea University
Seoul 02841, Republic of Korea

S. Park
Department of Materials Science and Engineering
Korea Advanced Institute of Science and Technology (KAIST)
Daejeon 34141, Republic of Korea

J. Lee
Department of Materials Science and Engineering
Pohang University of Science and Technology (POSTECH)
Pohang 37673, Republic of Korea

L. Gu
Department of Materials Science and Engineering and Institute for
NanoBioTechnology
Johns Hopkins University
Baltimore, MD 21218, USA

 The ORCID identification number(s) for the author(s) of this article can be found under <https://doi.org/10.1002/adma.202110340>.

DOI: 10.1002/adma.202110340

fibrosis, and others.^[18] FN presents a tripeptide amino acid sequence of Arg–Gly–Asp (RGD) in its heterogeneous intramolecular and intermolecular geometry that ligates to integrin receptors to facilitate cell adhesion formation in vivo. FN, which consists of several intramolecular domains, has a length and width of ≈ 16 and 9 nm, respectively.^[19,20]

Cell adhesion^[21–23] occurs when integrin recognizes and binds to the RGD loops on the FN-III₁₀ module, which are intramolecularly present in the FN exhibiting a dimension of 3 nm in the native and equilibrated state.^[19] Mechanical stretching of FN-III₁₀ module in vivo can elevate the dimension to 6 nm in the functionally decoupled state and 9 nm when the first β -strand separates. In this elevated dimension of 6–9 nm, integrin binding to the FN is known to be modulated, and the dimension of FN can increase up to 16 nm. These reports collectively suggest that tuning the submolecular ligand size and spacing can facilitate or inhibit the binding of integrin molecules to the differently sized and spaced ligands. This submolecular tuning of ligand size and spacing would thus elucidate the regulation of adhesion formation and immunomodulatory polarization of host macrophages.

Modulating ligand nanoassembly^[24–26] arrays presenting integrin-binding ligands can help to decipher the complex interplay between macrophages and ligand-presenting biomaterials,^[27–31] which governs the early host responses that proportionately leads to the long-term host responses.^[32,33] Integrin ligation-mediated downstream signaling stimulates the assembly of cytoskeletal actin and protein complexes involving myosin II, paxillin, and rho-associated protein kinase (ROCK) in adherent macrophages with an elongated shape,^[34] which leads to the anti-inflammatory/pro-healing M2 phenotype.^[35–38] In contrast, poor integrin ligation does not stimulate adhesion assembly

formation that results in the inflammatory M1 phenotype. Liganded gold nanoparticles (GNPs) patterned on a material surface can modulate cell adhesion^[39] by changing the ligand spacing and density,^[40] local versus global ligand density,^[41] ligand ordering,^[42] ligand micropattern,^[43] ligand clustering,^[44] and ligand geometry.^[45] In these ligand arrays, the spacing between neighboring liganded GNPs (≈ 10 nm in size) of less than 60–70 nm promotes cellular adhesion formation.^[40,41,45,46] Recently, it has been shown that closely spaced (40–110 nm) thin liganded line pairs are more effectively bridged by the integrin clusters than sparsely spaced thick liganded lines.^[47] However, regulating the binding of integrin to ligand arrays by varying the size and spacing of the ligand according to the intramolecular-scale dimensions of FN (16 nm) and integrin (10 nm) has not previously been reported.

In this study, we used nano-magnetite templates to localize densely packed liganded GNPs on the template surface with the in situ independent tuning of the size and edge-to-edge spacing (“7–3”, “7–18”, “13–17”, and “20–20”) of the liganded GNPs on both the intramolecular and intermolecular scale (**Scheme 1**). Herein, we use the notation “A–B”, where “A” refers to the liganded GNP size in nm and “B” refers to the liganded GNP edge-to-edge spacing in nm. Compared to previous studies on presenting liganded GNPs in arrays,^[40,41,45,46] we used comparable ranges of liganded GNP density (the number of GNPs per μm^2) in the arrays but localized liganded GNPs on nano-magnetite templates to sensitively change integrin-ligand binding at both the intramolecular and intermolecular scale, which effectively regulated macrophage adhesion formation. We also tuned the ligand size and spacing on nano-magnetite templates such that the ligand spacing proportionally increases when increasing the ligand size while maintaining the ligand density on the surface of both the templates and the entire material surface for all the compared groups.

Since the integrin head size is ≈ 10 nm, each liganded GNP of 7 nm (“7–3”) and 13 nm (“13–17”) in size functioned to roughly accommodate integrin. In contrast, each 20 nm-sized liganded GNP (“20–20”) offers binding sites for multiple integrin molecules. Interestingly, 7 nm liganded GNP size and 3 nm edge-to-edge spacing of neighboring liganded GNPs, both of which lie within the submolecular dimension of the FN, facilitate the binding of integrin molecules to liganded GNPs to form integrin clusters. In this regard, we refer to this group (“7–3”) as submolecular ligand arrays for integrin ligation. Our findings suggest that these submolecular ligand arrays can facilitate saturated integrin clustering that robustly induces macrophage adhesion similarly to the liganded gold shells. Our present study of planar ligand arrays on the submolecular scale that modulate the binding of integrin to the ligands advances from the recent findings of multiple integrins bridging 1D ligands that are widely spaced (slightly below 110 nm).^[47] In contrast, 16 nm edge-to-edge spacing of neighboring liganded GNPs suppresses integrin binding and clustering, and thus macrophage adhesion, in the “7–18” and “13–17” groups. However, when multiple integrin molecules could bind to each 20 nm-sized liganded GNPs (“20–20”), integrin binding and clustering and macrophage adhesion were slightly elevated.

As the ECM undergoes continuous remodeling to dynamically present heterogeneously organized ligands within the

D.-H. Kim

Department of Radiology
Feinberg School of Medicine
Northwestern University
Chicago, IL 60611, USA

T.-H. Kim

School of Integrative Engineering
Chung-Ang University
Seoul 06974, Republic of Korea

R. Paulmurugan

Department of Radiology
Molecular Imaging Program at Stanford
Stanford University School of Medicine
Stanford University
Palo Alto, CA 94304, USA
E-mail: paulmur8@stanford.edu

R. Paulmurugan

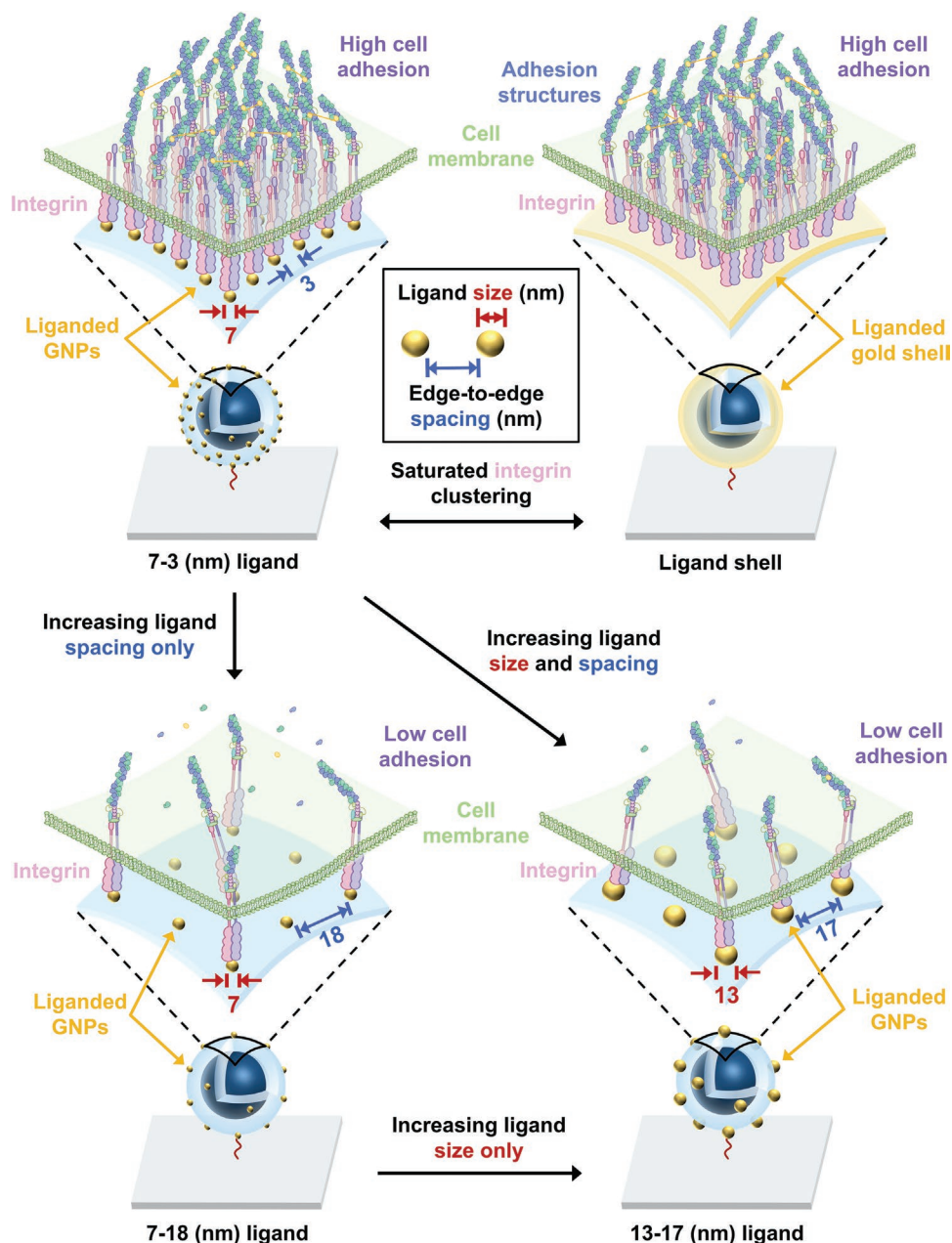
Department of Radiology
Canary Center at Stanford for Cancer Early Detection
Stanford University School of Medicine
Stanford University
Palo Alto, CA 94304, USA

H. Kang

Department of Biomicrosystem Technology
Korea University
Seoul 02841, Republic of Korea

H. Kang

Institute of Green Manufacturing Technology
Korea University
Seoul 02841, Republic of Korea



Scheme 1. Schematic of submolecular tuning ligand size and spacing to regulate integrin binding and clustering. Descriptions of the proposed model of independently unraveling the effect of ligand size and spacing on integrin ligation and the clustering of macrophages: “7–18”, “13–17”, “7–3”, and “gold shell”. In the “A–B” notation, “A” indicates the liganded GNP size in nm and “B” indicates the liganded GNP edge-to-edge spacing in nm. The “7–3” arrays stimulate the binding of integrin across neighboring liganded GNPs, resulting in robust macrophage adhesion comparable to fully liganded gold shells as a positive control. Relative to the “7–3” ligand arrays, increasing the “ligand spacing only” or “both ligand size and spacing” in the “7–18” and “13–17” liganded sites, respectively, yields binding sites for integrin but suppresses multiple integrin molecules joining the neighboring liganded sites due to the “ligand spacing” playing a dominant role, resulting in poor macrophage adhesion.

FN-bearing 3D structure,^[48] dynamically and axially displacing planar ligand arrays^[49] can mimic the 3D dynamics of native FN. Indeed, we used a pliable linker to conjugate the nano-magnetic templates presenting ligand arrays of various ligand sizes and spacing on the material surface such that magnetically attracting the nano-magnetic templates can shift the ligand arrays toward the material surface and anchor them. This dynamically stimulated anchoring of the ligand arrays in

the “20–20” group could stabilize multiple integrin molecules to “stably” bind to 20 nm-sized liganded GNP to promote integrin clustering, adhesion formation, and M2 polarization of host macrophages *in vivo* (due to the magnetic field that can readily penetrate tissues)^[50–53] at a comparable level to that of the “7–3” group. These findings are in accordance with a recent report on multiple integrin molecules “statically” bridging 1D ligand structures^[47] and are set apart from our own recent

reports revealing the magnetic manipulation of 1D ligand structures of nanocoils^[54] and nanobarcodes^[55] as well as ligand-blocking structures.^[56]

2. Results and Discussion

2.1. Submolecular Ligand Size and Spacing in Nanoassemblies via In Situ GNP Growth

To tune the size and spacing of liganded GNPs on the intramolecular and intermolecular scale, we first synthesized various sizes of GNPs using a seed-mediated growth method. In particular, we prepared the “7–3” group where liganded GNP (7 nm in size) and edge-to-edge-spacing (3 nm) between adjacent liganded GNPs lie within the intramolecular dimension of the FN (16 nm) and integrin (10 nm) to examine its effect on the binding of integrin to form integrin clusters. We synthesized GNPs with sizes of 3 and 13 nm by tuning the Au³⁺ precursor concentration and reducing agents. Furthermore, we used 13 nm-sized GNPs to modulate the growth of larger GNPs with sizes of 20, 32, or 50 nm, that all exhibited homogeneous spherical shapes via seed mediated growth, as observed in transmission electron microscopy (TEM) images and analogous UV–vis absorption peaks at around 520 nm (Figure S1a–c, Supporting Information). To mediate the conjugation and in situ growth of the GNPs, nano-magnetic templates were functionalized via amino-silica coating. X-ray diffraction (XRD) spectra, vibrating sample magnetometry (VSM) measurements, and dynamic light scattering revealed that the magnetite (Fe₃O₄) phase and reversible magnetization of the nano-magnetite templates with a hydrodynamic diameter of 222 ± 5.7 nm after amino-silica coating (Figure S2a–d, Supporting Information).

Since the GNPs exhibit a minimum Debye length of 2.5–3.0 nm that varies depending on the Au³⁺ concentration and citrate to Au³⁺ ratio during their synthesis,^[57] the GNPs are expected to display inter-spacing of at least 5–6 nm due to the theoretical limit of repulsion. Consequently, distributing liganded GNPs below 6 nm edge-to-edge spacing which corresponds to the submolecular FN dimension could not be achieved. To overcome this constraint, we considered whether we could conjugate GNPs to aminated nano-magnetite templates via amine-gold bonding first and then subsequently use the conjugated GNPs as seeds to mediate the in situ growth of the GNPs on the nano-magnetite surface to achieve 3 nm edge-to-edge spacing between them. After conjugating the GNPs to the aminated nano-magnetite, the resulting GNP arrays were stabilized with polyvinylpyrrolidone (PVP). Afterward, we repeatedly supplied small amounts of Au³⁺ to prevent Au self-nucleation, thereby ensuring the preferential template-assisted in situ growth of the GNPs on the nano-magnetite surface instead of forming new individual GNPs. TEM images and UV–vis absorbance spectra confirmed the tightly modulated in situ growth of the 3 nm GNPs conjugated to the nano-magnetite to obtain 7, 9, and 11 nm GNP-conjugated nano-magnetites exhibiting red shifts in the absorption peaks with increasing sizes of the in situ grown GNPs (Figure S3a–c, Supporting Information).

We tuned the liganded GNP sizes and spacing in the “7–3”, “13–17”, and “20–20” groups while maintaining the liganded GNP density invariant. Specifically, we prepared the “20–20” group that provides binding sites on each 20 nm-sized liganded GNP for multiple integrin molecules. In contrast, the “7–3” and “13–17” groups can only accommodate single integrin molecule per liganded GNP. The elemental maps for gold, silicon, and iron elements and high-resolution TEM (HR-TEM) atomic-scale image confirmed the uniform in situ growth of the GNPs on the amino-silica-coated nano-magnetite surfaces of the “7–3”, “13–17”, and “20–20” groups (Figure S4, Supporting Information). High angle annular dark field-scanning transmission electron microscopy (HAADF-STEM) images, hydrodynamic diameter measurements, and UV–vis absorbance spectra confirmed the homogeneous in situ growth of GNPs on the nano-magnetite template surfaces of the “7–3”, “13–17” (12.5 ± 0.2 nm in size and 17.3 ± 1.0 nm edge-to-edge spacing), and “20–20” (20.3 ± 0.3 nm in size and 20.1 ± 1.0 nm edge-to-edge spacing) groups (Figure S5a–c, Supporting Information). XRD patterns and VSM measurements of the three groups showed the co-presence of both the crystalline Fe₃O₄ and Au phases and reversible magnetism, respectively (Figures S6 and S7, Supporting Information).

We controlled the size and spacing of the liganded GNPs. We used different densities of 3 nm-sized GNPs (the number of liganded GNPs per nano-magnetite template) as seeds on the nano-magnetite templates for in situ GNP growth (Figure S8a, Supporting Information). The “7–3” group (exhibiting 6.7 ± 0.1 nm in size and 2.8 ± 0.2 nm in edge-to-edge spacing) showed lower liganded GNP (edge-to-edge) spacing but identically sized homogeneously distributed GNPs compared with the “7–18” group (exhibiting 6.8 ± 0.1 nm in size and 17.8 ± 1.2 nm edge-to-edge spacing), as evidenced by HAADF-STEM images and corresponding elemental maps for iron (Fe) and gold (Au) elements present in the nano-magnetite (Fe₃O₄) and GNPs, respectively (Figure S8b, Supporting Information). We independently increased the size of the liganded GNPs while maintaining their spacing in the “7–18” group and the “13–17” group (Figure 1a). We also prepared “gold shells” by extensively inducing the in situ growth of GNPs on nano-magnetite templates to prepare fully liganded GNPs to be compared with the “7–3” group (Figures 1a, S8c, Supporting Information).

2.2. Submolecular Ligand Size and Spacing in GNP Arrays without Modulating the Nano-Magnetite Template Density

To present liganded GNP arrays of various ligand sizes and spacing on the intramolecular and intermolecular scales, nano-magnetite templates coated with GNP arrays were conjugated to the material surface using a pliable linker without modulating the nano-magnetite template density. This was employed to dynamically induce the axial displacement and anchoring of the ligand arrays to mimic the 3D ECM dynamics. The nano-magnetite templates presenting various GNP sizes and spacing were coated with a heterobifunctional pliable linker via GNP-thiol bonding (Figure S9, Supporting Information). The pliable linker-conjugated GNP arrays were then conjugated to

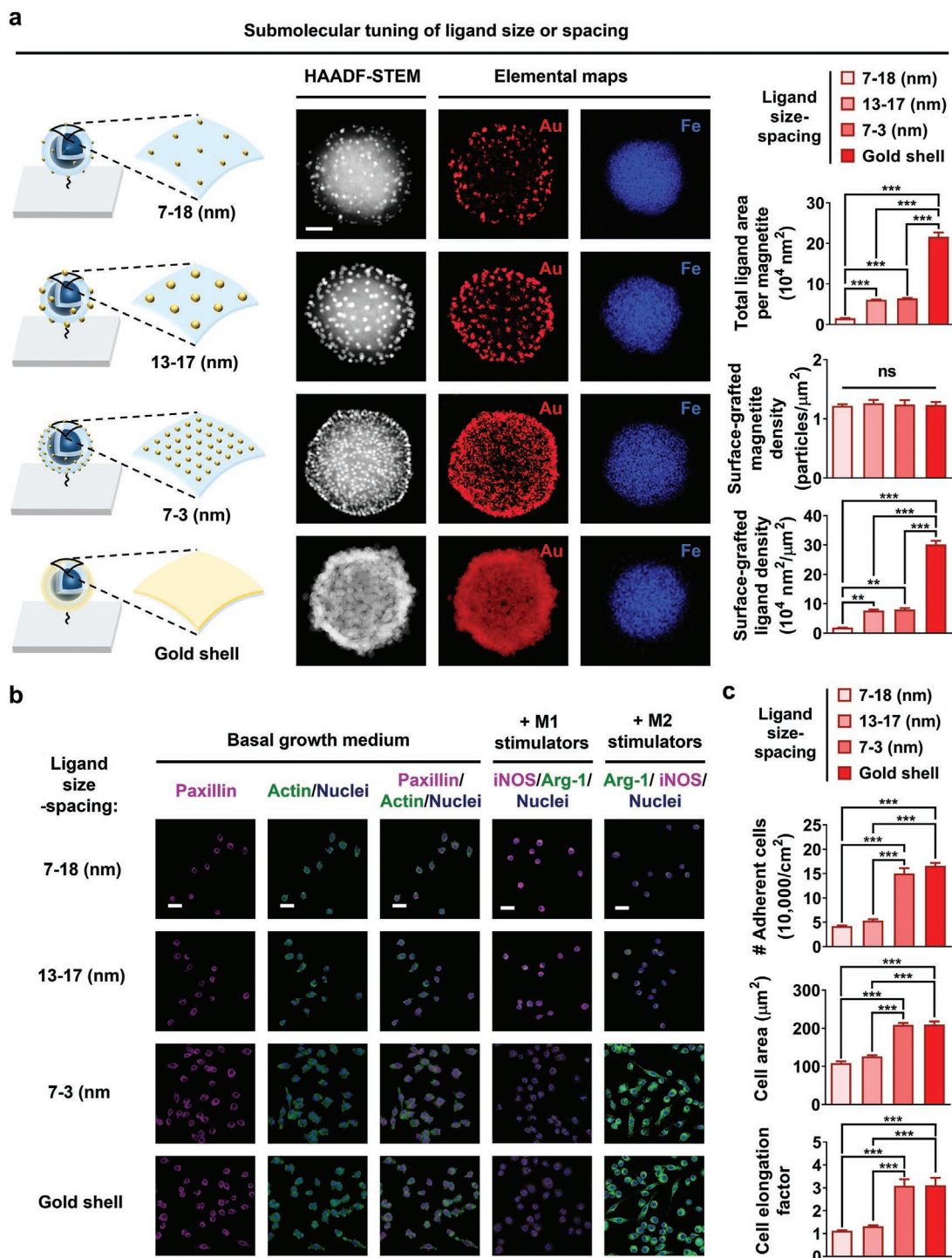


Figure 1. “7–3” ligand arrays with submolecular spacing facilitate robust macrophage adhesion and pro-regenerative polarization similar to “gold shell” ligand arrays. a) High-angle annular dark-field scanning transmission electron microscopy (HAADF-STEM) images, corresponding energy-dispersive spectroscopy (EDS)-based elemental maps of ligand arrays of various liganded GNP sizes and spacing. The iron (Fe) and gold (Au) elements were identified in the nano-magnetite (Fe₃O₄) and gold nanoparticles (GNPs), respectively. Scale bar: 50 nm. The groups with independently tuned ligand size and spacing are “7–18”, “13–17”, “7–3”, and “gold shell”. In the “A–B” notation, “A” indicates the liganded GNP size in nm and “B” indicates the liganded GNP edge-to-edge spacing in nm. Corresponding computations of the total area of liganded GNPs per nano-magnetite template, the surface-conjugated nano-magnetite density, and the surface-conjugated ligand density. b) Immunofluorescent staining images of F-actin, paxillin, nuclei, and an overlay of adhered macrophages after 24 h of culturing in basal medium and iNOS/Arg-1/nuclei overlay of adhered macrophages after 36 h of culturing in basal medium supplemented with either M1 or M2 polarization stimulators on the “7–18”, “13–17”, “7–3”, or “gold shell” groups. Scale bars: 20 μm. Corresponding computations of the number, area, and elongation factor of adhered macrophages are also included. Data are presented as the mean ± standard error (*n* = 5). Asterisks are assigned to *p* values with statistical significances for multiple groups compared by one-way analysis of variance with Tukey–Kramer post-hoc tests (**: *p* < 0.01; ***: *p* < 0.001). ns denotes statistically nonsignificant differences.

the aminated material surface via the EDC/NHS reaction by tuning the reaction time for the “7–3”, “13–17”, and “20–20” groups such that they exhibited a similar number of homogeneously distributed nanotemplates and thus ligand density, as evidenced by scanning electron microscopy (SEM) images (Figure S10, Supporting Information). The areas not covered with liganded GNP arrays were passivated to induce the ligand array-specific regulation of integrin binding and macrophage adhesion formation. The EDC/NHS-activated pliable linker-conjugated GNP arrays on the material surface reacted with the amine group of a lysine residue in the cyclic RGD ligand to complete the construction of the liganded GNP arrays, which was revealed by Fourier transform infrared spectroscopy demonstrating sequential changes in chemical bonds (Figure S11, Supporting Information). For the “7–18” group exhibiting lower liganded GNP density and the “gold shell” group exhibiting higher liganded GNP density than those of the “7–3”, “13–17”, and “20–20” groups, the pliable linker-conjugated GNP arrays were coupled to the material surface by reacting them for different time periods. Multiplying the total area of liganded GNPs per nano-magnetite template by the number of nano-magnetite templates per unit area yielded surface-conjugated ligand densities of $1.85 \times 10^4 \pm 0.01 \times 10^4$, $7.69 \times 10^4 \pm 0.35 \times 10^4$, $8.03 \times 10^4 \pm 0.49 \times 10^4$, and $30.14 \times 10^4 \pm 1.31 \times 10^4 \text{ nm}^2 \mu\text{m}^{-2}$ for the “7–18”, “13–17”, “7–3”, and “gold shell” groups, respectively (Figure 1a). In particular, the ligand density was significantly higher (by 275%) in the “gold shell” group than in the “7–3” group. These findings prove the independent tuning of ligand size and spacing with an invariant nano-magnetite density in these four groups.

2.3. Submolecular Spacing and Gold Shell of the Ligands Similarly Facilitate the Adhesion-Aided Pro-Regenerative Polarization of Macrophages

We proved the effect of independently tuning the ligand size and spacing in the “7–18”, “13–17”, “7–3”, and “gold-shell” groups on the regulation of adhesion formation of macrophages after 24 h of culturing macrophages. Immunofluorescent staining images and following quantifications of adhesion density, spread area, and elongated morphology show that pervasive assemblies of macrophage F-actin and paxillin adhesion complexes were significantly higher in the “7–3” and “gold shell” groups compared to the “7–18” and “13–17” groups, which exhibited minimal assemblies (Figure 1b,c and Figure S12, Supporting Information). These findings confirm that the “7–3” group stimulates adhesion formation of macrophages at a level comparable to that of the “gold shell” group. In contrast, independently increasing the ligand edge-to-edge spacing from 3 nm (the “7–3” group) to 18 nm (the “7–18” group) significantly reduced macrophage adhesion formation. Furthermore, independently increasing the ligand size from 7 nm (the “7–18” group) to 13 nm (the “13–17” group) while maintaining similar ligand spacing (17–18 nm) did not augment macrophage adhesion formation. This outcome suggests that ligand spacing in this range of ligand size and spacing played a dominant role in regulating macrophage adhesion.

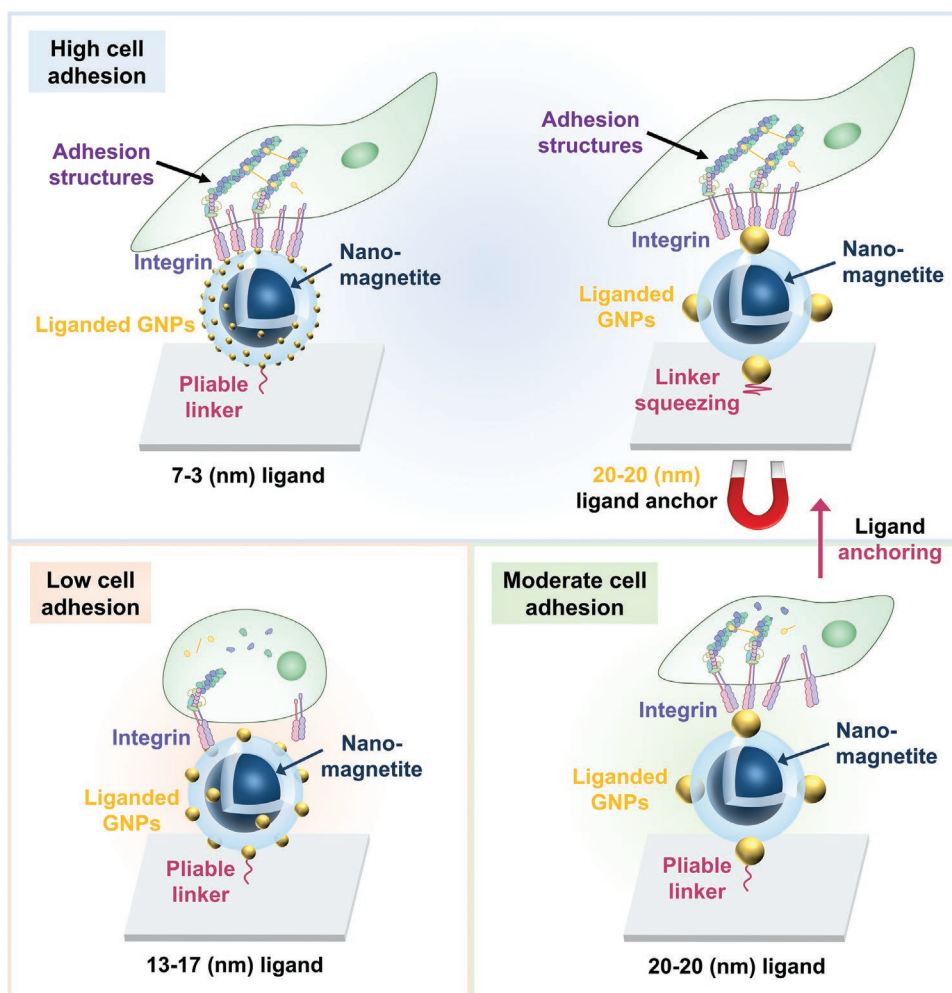
Since robust cytoskeletal adhesion formation of macrophages with elongated morphology involving ROCK signaling^[34,35]

leads to anti-inflammatory/pro-healing M2 polarization while hindering pro-inflammatory M1 polarization, we next pondered whether the “7–3” and the “gold shell” groups exhibit adhesion-assisted M2 polarization. Macrophages were cultured with each of the four liganded GNP groups in the presence of M1 or M2 polarization-inducing stimulators for 36 h and analyzed for either M1 or M2 polarization, respectively. Immunofluorescent staining images of the “7–3” and “gold shell” groups demonstrated pervasive expression of M2 polarization marker (Arg-1) in the presence of M2 stimulators but minimal expression of M1 polarization marker (iNOS) despite the presence of M1 stimulators (Figure 1b). Conversely, immunofluorescent staining images of the “7–18” and “13–17” groups indicated extensive expression of iNOS in the presence of M1 stimulators but minimal expression of Arg-1 despite the presence of M2 stimulators. These results prove that both the “7–3” and “gold shell” groups analogously stimulate the adhesion formation of macrophages to mediate M2 polarization and restrain M1 polarization. When ligands are far apart, the adhesion formation of macrophages is suppressed, which leads to pronounced M1 polarization.

2.4. Increasing Ligand Spacing Dominantly Limits Integrin Clustering Independent of the Ligand Density

We next considered whether tuning of ligand size and spacing in the “7–3”, “13–17”, and “20–20” groups at invariant ligand density can regulate integrin binding and clustering (Scheme 2, Figure 2a). Similar to previous reports that present liganded GNPs in arrays,^[40,41,45,46] we used comparable liganded GNP densities of ≈ 560 , 140, and 59 GNPs/ μm^2 for the “7–3”, “13–17”, and “20–20” groups, respectively (Figure 2b). The calculated surface-conjugated ligand densities in the “7–3”, “13–17”, and “20–20” groups were similar (in the range from 6.91×10^4 to 7.65×10^4 ligands/ μm^2), thereby proving the ligand-density-independent tuning of ligand size and spacing (Figure 2c).

We next examined the efficiency of integrin $\beta 1$ binding and clustering to ligand arrays by placing the ligand arrays in integrin $\beta 1$. Immunofluorescent staining images of integrin $\beta 1$ clusters and fluorescence intensity quantification show that integrin $\beta 1$ was markedly clustered in the “7–3” group, slightly clustered in the “20–20” group, and negligibly clustered in the “13–17” group (Figure S13a,b, Supporting Information). Furthermore, the effect of tuning the ligand size and spacing on the binding of integrin was analyzed via immunolabeling using (secondary antibody-coated) GNPs to label (primary antibody-coated) integrins bound to the liganded GNP arrays (Figure S14, Supporting Information). SEM images and quantification of GNP-labeled integrin $\beta 1$ per nano-magnetite template of adherent macrophages after 24 h of culturing highlighted that integrin $\beta 1$ was substantially clustered in the “7–3” group, slightly clustered in the “20–20” group, and minimally to negligibly clustered in the “13–17” group (Figure 2d). At the primal stage of macrophage plating (before adhesion), cells recognize similar contact area for adhesion which presents similar GNP array densities as revealed by SEM and energy-dispersive spectroscopy (EDS) imaging and quantifications regardless of the groups as the ligand density among them (the “7–3”, “13–17”,



Scheme 2. A schematic representation of tuning the ligand size and spacing with constant ligand density to regulate integrin ligation and clustering. Descriptions of the effect of ligand size and spacing on integrin binding and clustering and the resultant polarization of macrophages by the “7–3”, “13–17”, and “20–20” ligand arrays. The “7–3” ligand arrays facilitate integrin binding and clustering, thereby stimulating macrophage adhesion formation. The “13–17” ligand arrays limit multiple integrin molecules from clustering across the neighboring liganded sites, thus suppressing macrophage adhesion formation. The “20–20” ligand arrays enable multiple integrin molecules to simultaneously bind to each large-sized liganded site, thereby slightly elevating the chance of integrin clustering. Dynamic stimulation of “20–20, + Anchor” ligand arrays stabilizes integrin clustering, which strengthens macrophage adhesion formation.

and “20–20” groups) are comparable (Figure S15a,b, Supporting Information).^[58] However, due to the difference in the degree of clustered integrin to the ligand arrays that results from the tuning of ligand size and spacing, cell spreading in various groups differed and thus total number of ligand arrays recognized per cell differed. Immunofluorescent staining images of integrin $\beta 1$ in adherent macrophages corroborated the trend observed in the immunolabeling experiment (Figure 3a).

Immunofluorescent staining images also show a consistent trend in the differing levels of assemblies of F-actin, paxillin, and vinculin adhesion complexes in the macrophages: the highest was in the “7–3” group, moderate in the “20–20” group, and the lowest in the “13–17” group (Figure 3a and Figure S16a, Supporting Information). Computations of adhesion density, spread area, and elongated morphology in the groups followed the same trend (Figure 3b and Figure S16b, Supporting Information). To confirm the effect of increasing the densities

of ligand arrays for macrophage adhesion, we prepared “7–3”, “13–17”, and “20–20” groups in three different ligand array densities each (thereby controlling the total ligand densities) by modulating the reaction time of GNP arrays conjugation to the substrate. The uniform distribution of ligand arrays in all groups was evidenced by the SEM images (Figure S17a, Supporting Information). In “7–3” group, the number of nano-magnetites per μm^2 increased as 1.23 ± 0.07 , 2.43 ± 0.07 , and 3.56 ± 0.07 with the increase of reaction time, respectively. Similarly, “13–17” presented 1.22 ± 0.06 , 2.61 ± 0.04 , and 3.74 ± 0.13 nano-magnetites per μm^2 , and “20–20” groups resulted in 1.22 ± 0.04 , 2.34 ± 0.04 , and 3.50 ± 0.06 nano-magnetites per μm^2 . Based on the number of nano-magnetites per μm^2 , groups were labeled as “Density 1x” (1.1–1.3 ligand arrays per μm^2), “Density 2x” (2.3–2.6 ligand arrays per μm^2), and “Density 3x” (3.3–3.7 ligand arrays per μm^2) for the “7–3”, “13–17”, and “20–20” groups (Figure S17a,b, Supporting Information). In

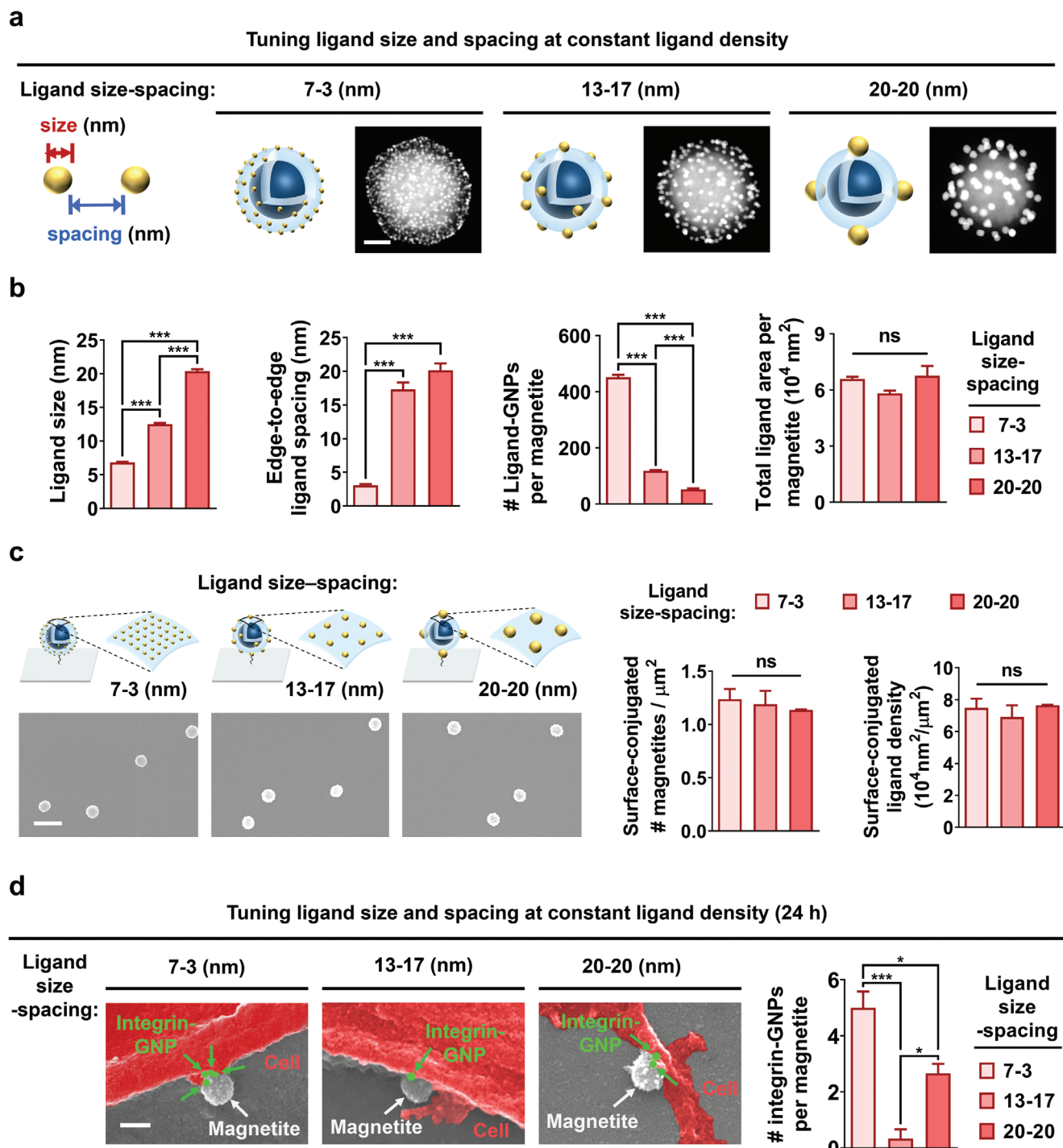


Figure 2. Increasing ligand spacing dominantly limits integrin binding and clustering independently of the ligand density. a) HAADF-STEM images of the ligand arrays on various liganded GNP sizes and spacing while keeping the ligand density constant. Scale bar: 50 nm. b) Corresponding computations of liganded GNP size, edge-to-edge ligand spacing, the number of liganded GNPs per nano-magnetite template, and the total area of liganded GNPs per nano-magnetite template. c) SEM images of various liganded arrays and corresponding computations of surface-conjugated nano-magnetite density and surface-conjugated ligand density. Scale bar: 500 nm. d) immunolabeling and SEM images of macrophage adhesion formation (red) after 24 h of culturing highlighting integrin $\beta 1$ binding that occurs on the ligand arrays via immunolabeling of integrin $\beta 1$ with GNPs (green) and computed number of integrin $\beta 1$ -labeled GNPs per nano-magnetite template (gray). Scale bar: 200 nm. The groups with tuned ligand sizes and spacing independently of the ligand density are “7–3”, “13–17”, and “20–20”. In the “A–B” notation, “A” indicates the liganded GNP size in nm and “B” indicates the liganded GNP edge-to-edge spacing in nm. Data are displayed as the mean \pm standard error ($n = 10$). Asterisks are assigned to p values with statistical significances for multiple groups compared by one-way analysis of variance with Tukey–Kramer post-hoc tests (*: $p < 0.05$; ***: $p < 0.001$). ns indicates statistically nonsignificant differences.

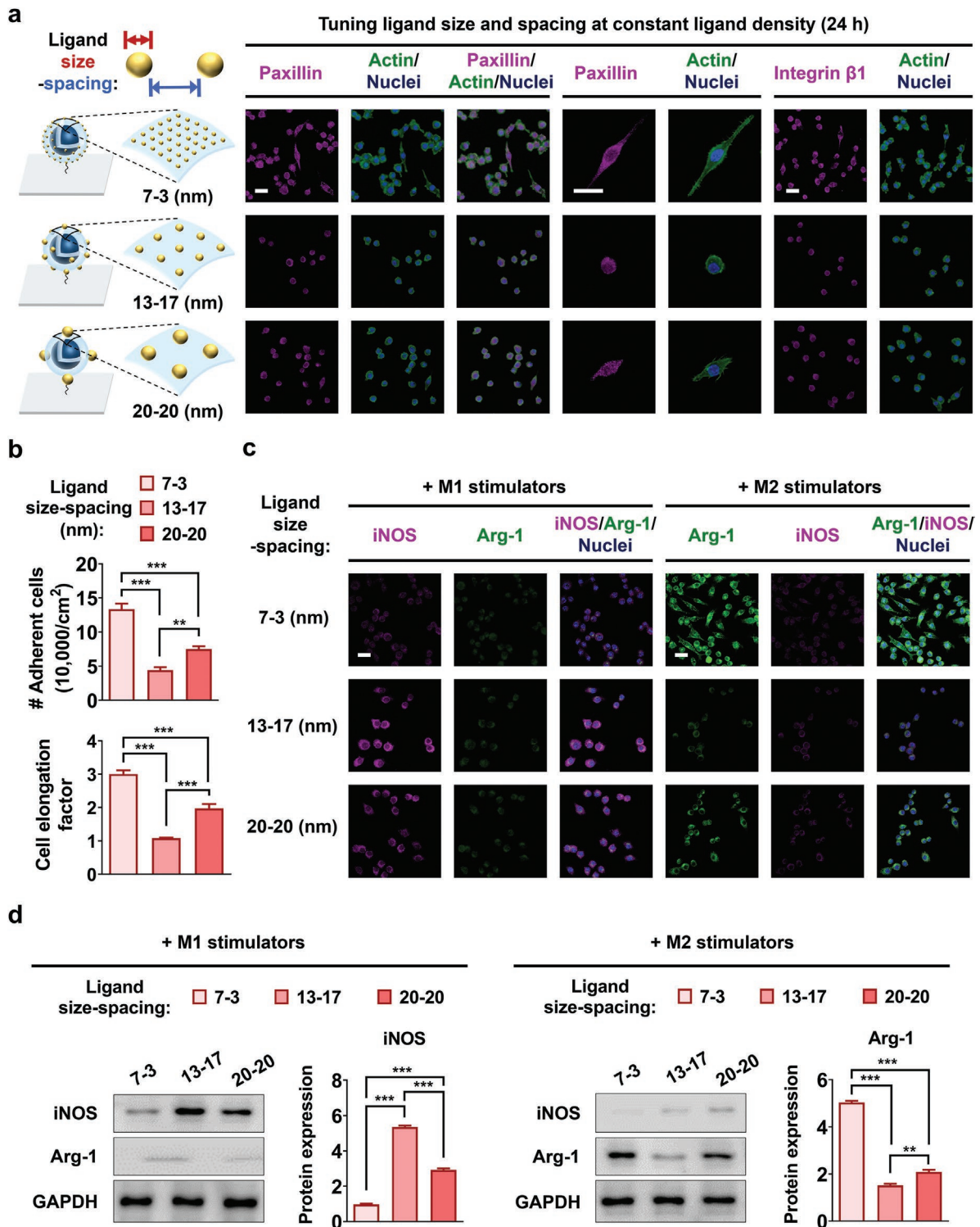


Figure 3. Increasing ligand spacing dominantly without modulating the ligand density hinders integrin-clustering-dependent macrophage adhesion formation and pro-healing polarization but stimulates pro-inflammatory polarization. a) Immunofluorescent staining images of paxillin or integrin $\beta 1$ along with F-actin, nuclei, and an overlay of adhered macrophages after 24 h of culturing in basal medium on the “7–3”, “13–17”, or “20–20” group. In the “A–B” notation, “A” indicates the liganded GNP size in nm and “B” indicates the liganded GNP edge-to-edge spacing in nm. b) Corresponding computations of the number and elongation factor of adhered macrophages from the acquired images in a). c) Immunofluorescent staining images and d) western blotting imaging with corresponding computations of protein expression levels of M1 marker (iNOS) and M2 marker (Arg-1) after normalization to that of GAPDH for adhered macrophages after 36 h of culturing in basal medium supplemented with M1 or M2 polarization stimulators, respectively. Scale bars: 20 μ m. Data are presented as the mean \pm standard error ($n = 5$). Asterisks are assigned to p values with statistical significances for multiple groups compared by one-way analysis of variance with Tukey–Kramer post-hoc tests (**: $p < 0.01$; ***: $p < 0.001$).

proportion to the increase of ligand arrays on the substrate, surface-conjugated ligand densities also increased approximately by two and three times each than the “Density 1x” group for the “Density 2x” and “Density 3x” groups, respectively. Moreover, the inter-distance between the ligand arrays decreased in an inversely proportionate manner (Figure S17b, Supporting Information). Immunofluorescent staining images of paxillin along with F-actin and nuclei of adhered macrophages after 24 h of culturing in basal medium on “Density 2x” groups showed markedly higher adhesion in all groups than the cells cultured on “Density 1x” groups (Figure 3a,b, Figures S16b and S18a,b, Supporting Information). Notably, “Density 2x” was sufficient to show saturated effect of macrophage adhesion in all groups, suggesting that any density higher to yield insignificant results. In negative control experiments, the adhesion formation of macrophages was evaluated after tuning the GNP size and spacing under two conditions: without RGD ligand conjugation and with scrambled ligand sequence conjugation. Both exhibited poor adhesion formation in macrophages without considerable differences between the groups, thus proving that integrin-specific RGD ligand sequences are indispensable for the ligand size- and spacing-regulated integrin binding and clustering in macrophage adhesion (Figures S19a,b and S20a,b, Supporting Information). When cultured in the presence of M2 polarization stimulators, immunofluorescent staining images and western blotting analysis confirmed that the expression of Arg-1 was the highest in the “7–3” group, moderate in the “20–20” group, and the lowest in the “13–17” group whereas the expression of iNOS showed the opposite trend (Figure 3c,d and Figure S21a,b, Supporting Information). These findings collectively prove that with invariant ligand density, the “7–3” group significantly facilitated integrin binding and clustering along with macrophage-adhesion-aided M2 polarization and restrains M1 polarization. The “13–17” group attained the opposite results, i.e., integrin binding, clustering, and macrophage-adhesion-assisted M2 polarization were inhibited while M1 polarization was strengthened. The trend for the “20–20” group was between the “7–3” and “13–17” groups.

Since 3 nm edge-to-edge spacing of liganded GNPs in the “7–3” group lies within the submolecular dimension of FN and integrin, it is most probable that the binding of integrin (10 nm in size) is facilitated across the adjacent liganded GNPs spaced at 3 nm. This could be due to macrophages forming saturated integrin clusters, which facilitate adhesion formation-assisted anti-inflammatory/pro-healing M2 polarization. The level of this effect is similar to that shown by the “gold shell” ligands that exhibit a significantly higher (by 275%) material surface-conjugated ligand density compared to the “7–3” group (Figure 1a-c). In contrast to a recent study in which many integrins bridged highly dense 1D ligands spaced below 110 nm,^[47] we provide novel findings by utilizing submolecular spacing in the ligation of integrin while using a comparable range of liganded GNP density used in most of the recent studies. The ligand dimension and distribution in the “7–18” and the “13–17” groups fall slightly outside of the FN dimension (≈ 16 nm). Moreover, our results show that the binding of integrin molecules to the ligand sites with spacing larger than 16 nm is highly inhibited, such that the macrophages perceive these ligands far apart. Consequently, the integrin clustering

and adhesion formation are limited to result in inflammatory M1 polarization. Even though the liganded GNP size is significantly higher in the “13–17” group than in the “7–18” group (albeit with similar spacing), these two groups showed similar degrees of macrophage adhesion. These findings substantiate that ligand spacing is the predominant factor over ligand size. Interestingly, when the liganded GNP size was increased to 20 nm (the “20–20” group), integrin clustering and adhesion formation-mediated anti-inflammatory M2 polarization of macrophages were slightly facilitated with statistically significant differences compared to the “13–17” group despite the slightly higher spacing. This suggests that 20 nm is the threshold ligand size for promoting cell adhesion, which could be attributed to multiple integrin molecules binding to each 20 nm-sized ligands, thereby augmenting integrin clustering. This is in accordance with a recent report showing that thick liganded 1D lines slightly promoted cell adhesion slightly better than thin liganded 1D lines.^[47] Taken together, we deduce that ligand size, albeit less important than ligand spacing, also plays a role in determining integrin binding and clustering.

2.5. Dynamic Stimulation of Ligand Anchoring Strengthens Macrophage Adhesion despite Large Spacing of the Ligands

Since the FN-bearing 3D ECM continuously remodels itself to dynamically present ligands, we hypothesized that emulating these 3D dynamics could change the adhesion of macrophages to the ligand arrays via the axial displacement of the latter using the pliable linker.^[59] Hence, we used the “20–20” group that exhibited slight macrophage adhesion to examine the effect of dynamically anchoring the ligand on macrophage adhesion by placing a permanent magnet at the bottom of the material (Scheme 2, Figure S22a, Supporting Information). We carried out atomic force microscopy (AFM) imaging of an identical area of a ligand array under magnetic attraction downward to induce ligand anchoring (“+ Anchor”) by squeezing the pliable linker or loosening it in by not applying the magnet (“– Anchor”). The AFM images exhibit that the dark contrast areas of the magnetite presenting ligand arrays in the “+ Anchor” group were significantly lower in height and range in the gradient bar (211.3 ± 4.2 nm) than the “– Anchor” group (220.7 ± 3.2 nm) while its lateral size remained invariant (Figure S22a, Supporting Information).

Immunofluorescent staining images showed widespread assemblies of integrin $\beta 1$, F-actin, and paxillin adhesion complexes with significantly higher adherent cell numbers, spread area, and elongated morphology in the “+ Anchor” group compared with the “– Anchor” group (Figure S22b,c, Supporting Information). Concomitantly, significantly higher Arg-1 expression was observed in the “+ Anchor” group compared with that in the “– Anchor” group in the presence of M2 stimulators as proved by the immunofluorescent staining and western blotting images (Figures S22b–e and S23, Supporting Information). In contrast, significantly higher iNOS expression was observed in the “– Anchor” group compared with that in the “+ Anchor” group in the presence of M1 stimulators. This dynamic anchoring-regulated macrophage polarization required corresponding polarization-specific stimulators

(Figure S24a,b, Supporting Information). Our findings prove that dynamic stimulation of ligand anchoring facilitates integrin clustering across the ligands far apart, which mediates macrophage-adhesion-aided M2 polarization. The pliable linker^[60,61] was anchored to or loosened from the material surface via axial shifting to produce a height difference of 9.4 nm (Figure S22a, Supporting Information). The anchoring “stabilized” the binding of multiple integrin molecules to each 20 nm-sized ligand, which stimulated integrin clustering, thereby facilitating adhesion formation and M2 polarization levels. Our approach can mimic the 3D dynamics of heterogeneously organized ligands in native FN by manipulating the lateral and axial ligand distributions on the intramolecular and intermolecular scale to modulate integrin binding, stabilization, and clustering. Furthermore, modulating the in situ GNP growth to tune the ligand size and spacing on the intramolecular and intermolecular scale and synthesizing nano-magnetite templates of various sizes and shapes can offer limitless combinations of 3D dynamic ligand arrays to systematically investigate complex nanogeometry-dependent integrin binding and clustering.

The signaling pathway involving ROCK, actin polymerization, and myosin II has been reported to regulate the host responses such as pro-healing versus pro-inflammatory polarization of macrophages.^[34,35] We next investigated how macrophage adhesion formation regulates the polarization of macrophages under the influence of the various ligand arrays by using pharmacological inhibitors specific for ROCK (Y27632), actin polymerization (cytochalasin D), and myosin II (blebbistatin). Immunofluorescent staining images show that ROCK2 expression was considerably higher with the “7–3” group and anchoring of the “20–20, + Anchor” group than in the “13–17” and “20–20” groups (Figure S25, Supporting Information). In the presence of M1 stimulators, robust macrophage adhesion was observed with a substantially larger adherent cell area and elongated morphology in the “7–3” and “20–20, + Anchor” groups compared with the “13–17” and “20–20” groups (Figure S26a,b, Supporting Information). Furthermore, iNOS expression was minimal in the “7–3” and “20–20, + Anchor” groups but highly elevated in the presence of its inhibitors (Figure S26a,b, Supporting Information). Conversely, in the presence of M2 stimulators, Arg-1 expression was substantially higher in the “7–3” and “20–20, + Anchor” groups but diminished in the presence of its inhibitor (Figure S27a,b, Supporting Information). These results collectively reveal that both the “7–3” and “20–20, + Anchor” groups intensify macrophage adhesion involving molecular complexes of rho kinase, actin filaments, and myosin II, which augments M2 while hindering M1 polarization.

2.6. Ligand-Spacing- and Anchoring-Based Regulation of Host Macrophages In Vivo

We next pondered whether modulating the ligand size and spacing as well as anchoring at the intramolecular and intermolecular scales could also regulate integrin binding and clustering of recruited host macrophages in a dynamic in vivo microenvironment. We examined the early responses of

host macrophages after implantation as either inflammatory or tissue-healing.^[32,33] We subcutaneously implanted materials that are decorated with various ligand arrays (the ligand-density-independent “7–3”, “13–17”, and “20–20” groups) into mice and injected anti-inflammatory M2 stimulators onto the material surface to counteract the early inflammation-dominant response (Figure 4a). We also invoked the “20–20, + Anchor” group by attaching a permanent magnet to the abdomen side of the mice with the “20–20” group implant. We first examined the stability of the ligand arrays (i.e., nano-magnetite presenting liganded GNP arrays) in vivo. SEM imaging and subsequent computations confirmed that the ligand arrays remained intact without any sign of degradation and maintained similar densities at both pre-implantation and 24 h post-implantation (Figure S28a,b, Supporting Information). Both nano-magnetite and the application of a high-intensity magnetic field have been reported to be nontoxic to patients,^[62,63] which suggests the safe in vivo applicability of our ligand nanoarray and anchoring strategy.

We co-stained inflammatory M1 marker (iNOS) and pro-healing/anti-inflammatory M2 marker (Arg-1) along with F-actin and nuclei to identify the host macrophages. Pervasive assemblies of F-actin complexes in higher adherent host cell numbers, spread area, and high-aspect-ratio shape were observed in the “7–3” and “20–20, + Anchor” groups; they also exhibited a significantly higher expression level of Arg-1 and a lower expression level of iNOS than those in the “13–17” and “20–20” groups (Figure 4b,c, Figure S29, Supporting Information). Flow cytometry histograms concordantly confirmed that inflammatory marker (CD68) was substantially more highly expressed in the “13–17” and “20–20” groups whereas anti-inflammatory marker (CD163) was considerably more highly expressed in the “7–3” and “20–20, + Anchor” groups (Figure 4b,c, Figure S29, Supporting Information). We also found that host cells positive for NIMP-R14 (which indicates that they are host neutrophils) were also recruited to the ligand nanoarrays by the early host response (Figure S30a,b, Supporting Information). These results collectively substantiate that the submolecular spacing of the ligands efficiently stimulates macrophage adhesion formation, which augments M2 while restraining M1 polarization of host macrophages. Strikingly, while the adhesion formation of host macrophages was not extensively observed in the “20–20” group, dynamically induced ligand anchoring in the “20–20, + Anchor” group elevated the level of host macrophage adhesion comparable to that of the “7–3” group. This suggests that the integrin clustering of recruited host cells is stabilized on the anchored ligand arrays in response.

3. Conclusion

We have harnessed in situ growth of gold nanoparticle (GNP) seed arrays on nano-magnetite templates to independently tune the liganded GNP size and spacing from 3 to 20 nm on both the intramolecular and intermolecular scales. The 3 nm-spaced ligands facilitated the binding of integrin across neighboring ligands and thus saturated clustering, which mediated macrophage-adhesion-assisted pro-regenerative polarization. Increasing the ligand spacing induced macrophages

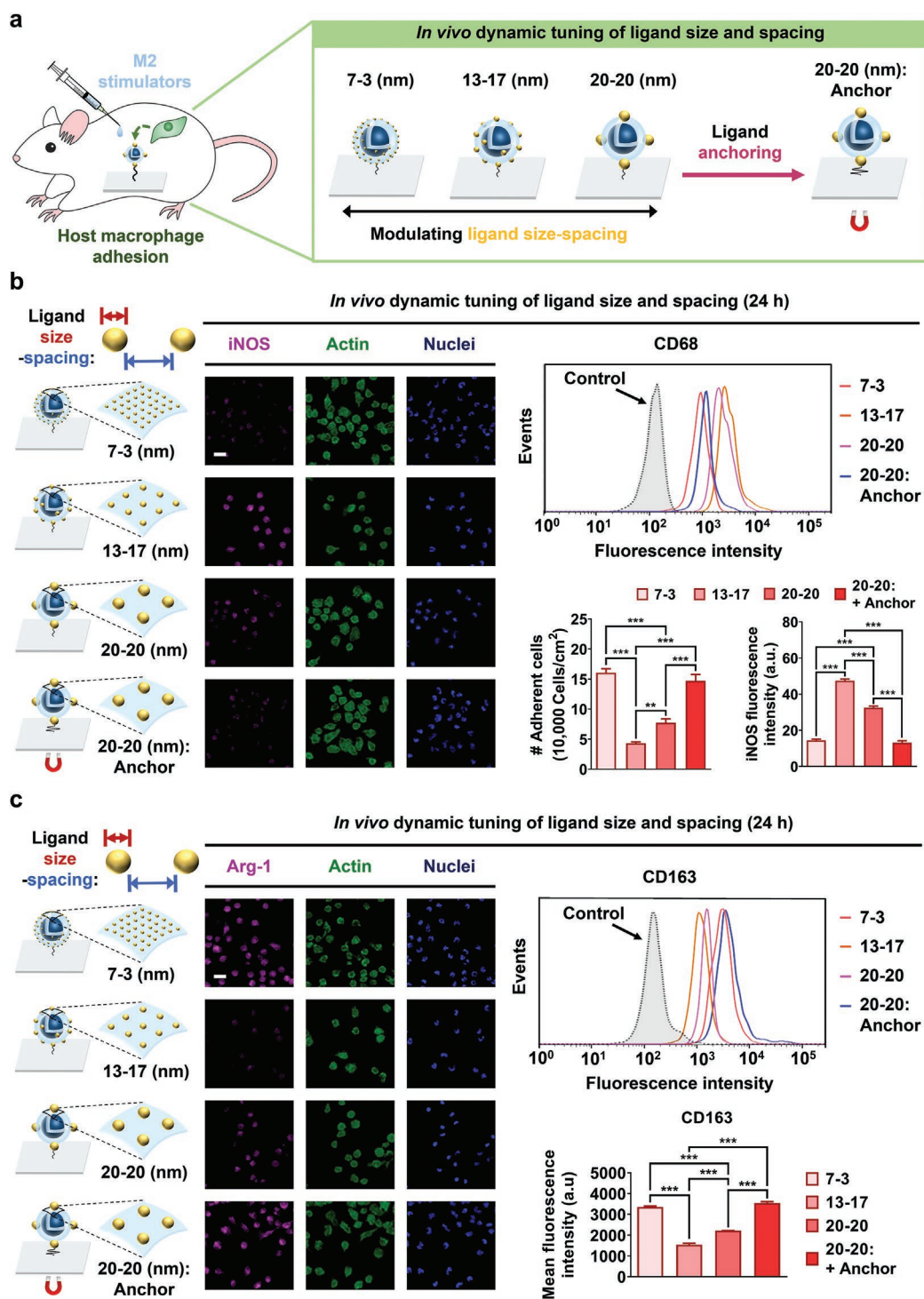


Figure 4. Both submolecular spacing and dynamic anchoring of ligands augment macrophage adhesion formation assisted anti-inflammatory polarization in vivo. a) A schematic representation of regulating host macrophages on the material decorated with various ligand arrays implanted into subcutaneous pockets of mice followed by injecting M2 polarization stimulators. b) In vivo immunofluorescent staining images of inflammatory M1 marker (iNOS) co-staining with F-actin and nuclei and flow cytometry histograms of inflammatory CD68 of adhered host cells at 24 h after implantation. Corresponding computations of adherent cell numbers and iNOS protein fluorescence intensities are included. c) In vivo immunofluorescent staining images of anti-inflammatory M2 marker (Arg-1) co-staining with F-actin and nuclei and flow cytometry histograms of anti-inflammatory CD163 and quantification of CD163 fluorescence intensities of adhered host cells at 24 h after implantation. The compared groups include “7–3”, “13–17”, “20–20”, and “20–20, + Anchor” (with a permanent magnet attached to the abdomen side of mice to induce ligand anchoring) groups. In the “A–B” notation, “A” indicates the liganded GNP size in nm and “B” indicates the liganded GNP edge-to-edge spacing in nm. The scale bars denote 20 μ m. Data are presented as the mean \pm standard error ($n = 6$). Asterisks are assigned to p values with statistical significances for multiple groups compared by one-way analysis of variance with Tukey–Kramer post-hoc tests (**: $p < 0.01$; ***: $p < 0.001$).

to recognize ligands far apart, thereby restraining integrin binding and clustering and thus macrophage adhesion, which yielded inflammatory polarization. Increasing the ligand size became effective at 20 nm as the threshold for promoting integrin-clustering-assisted macrophage adhesion formation. Finally, dynamic ligand anchoring induced stabilized integrin clustering of macrophages and thus triggered macrophage-adhesion-aided pro-healing polarization. Versatile tuning of the seed-mediated GNP growth, in situ GNP growth, and nanomagnetite templates in diverse sizes and shapes can offer 3D dynamic ligand arrays for immunoengineering.

Supporting Information

Supporting Information is available from the Wiley Online Library or from the author.

Acknowledgements

Y.K. and T.M.K. contributed equally to this work. This work was supported by the National Research Foundation of Korea (NRF) grant funded by the Korean government (MSIT) (No. 2020R1C1C1011038 and 2019R1A2C3006587). This work was also supported by a Korea University Grant and National Institutes of Health (grants numbers R01CA209888 and R21EB022298), NIH S10OD023518-01A1 Award for the Celigo S Imaging Cytometer (200-BFFL-S) to R.P., and Gary Glazer-GE Gift Fund (Department of Radiology, Stanford University). HAADF-STEM and fluorescence imaging (K1-fluo, Nanoscope System, Korea) was conducted with the support of the Seoul Center in Korea Basic Science Institute (KBSI) under the R&D programs (Project No. D110710) supervised by the Ministry of Science and ICT. Animal experiments in this study were conducted through approval from the Institutional Animal Care and Use Committee at Korea University (KOREA-2021-0006). This work made use of the EPIC facility of Northwestern University's NUANCE Center, which has received support from the Soft and Hybrid Nanotechnology Experimental (SHyNE) Resource (NSF ECCS-1542205), the MRSEC IRG2 program (NSF DMR-1720139) at the Materials Research Center, the International Institute for Nanotechnology (IIN), the Keck Foundation, and the State of Illinois, through the IIN.

Conflict of Interest

The authors declare no conflict of interest.

Data Availability Statement

The data that support the findings of this study are available from the corresponding author upon reasonable request.

Keywords

cell adhesion, ligand size, ligand spacing, macrophage modulation, nanoassemblies, submolecular ligands

Received: December 19, 2021
Revised: March 27, 2022
Published online: May 31, 2022

- [1] J. Che, A. Najer, A. K. Blakney, P. F. McKay, M. Bellahcene, C. W. Winter, A. Sintou, J. Tang, T. J. Keane, M. D. Schneider, *Adv. Mater.* **2020**, *32*, 2003598.
- [2] K. S. Kim, J. Y. Lee, J. Han, H. S. Hwang, J. Lee, K. Na, *Adv. Funct. Mater.* **2019**, *29*, 1900773.
- [3] M. S. Taha, G. M. Cresswell, J. Park, W. Lee, T. L. Ratliff, Y. Yeo, *Nano Lett.* **2019**, *19*, 8333.
- [4] J. K. Mouw, G. Q. Ou, V. M. Weaver, *Nat. Rev. Mol. Cell Biol.* **2014**, *15*, 771.
- [5] R. R. Bruns, W. Press, E. Engvall, R. Timpl, J. Gross, *J. Cell Biol.* **1986**, *103*, 393.
- [6] J. Li, X. Jiang, H. Li, M. Gelinsky, Z. Gu, *Adv. Mater.* **2021**, *33*, 2004172.
- [7] J. Fu, Y. Li, Y. Zhang, Y. Liang, Y. Zheng, Z. Li, S. Zhu, C. Li, Z. Cui, S. Wu, *Adv. Mater.* **2021**, *33*, 2102926.
- [8] Y. Wang, J. Yu, Z. Luo, Q. Shi, G. Liu, F. Wu, Z. Wang, Y. Huang, D. Zhou, *Adv. Mater.* **2021**, *33*, 2103497.
- [9] C. Cai, X. Zhang, Y. Li, X. Liu, S. Wang, M. Lu, X. Yan, L. Deng, S. Liu, F. Wang, F. Cunyi, *Adv. Mater.* **2022**, *34*, 2106564.
- [10] N. Qiu, G. Wang, J. Wang, Q. Zhou, M. Guo, Y. Wang, X. Hu, H. Zhou, R. Bai, M. You, *Adv. Mater.* **2021**, *33*, 2006189.
- [11] J. S. Lee, Y. H. Roh, Y. S. Choi, Y. Jin, E. J. Jeon, K. W. Bong, S.-W. Cho, *Adv. Funct. Mater.* **2019**, *29*, 1807803.
- [12] G. Digiacoio, I. Tusa, M. Bacci, M. G. Cipolleschi, P. Dello Sbarba, E. Rovida, *Cell Adhes. Migr.* **2017**, *11*, 327.
- [13] J. C. McCutcheon, S. P. Hart, M. Canning, K. Ross, M. J. Humphries, I. Dransfield, *J. Leukocyte Biol.* **1998**, *64*, 600.
- [14] K. Alitalo, T. Hovi, A. Vaheri, *J. Exp. Med.* **1980**, *151*, 602.
- [15] A. H. Sikkema, J. M. Stoffels, P. Wang, F. J. Basedow, R. Bultink, J. J. Bajramovic, W. Baron, *J. Neuroinflammation* **2018**, *15*, 218.
- [16] P. Sudhakaran, A. Radhika, S. Jacob, *Glycoconjugate J.* **2007**, *24*, 49.
- [17] M. Kang, J. Hong, M. Jung, S. P. Kwon, S. Y. Song, H. Y. Kim, J. R. Lee, S. Kang, J. Han, J. H. Koo, *Adv. Mater.* **2020**, *32*, 2003368.
- [18] W. J. Kao, D. Lee, *Biomaterials* **2001**, *22*, 2901.
- [19] V. E. Koteliansky, M. A. Glukhova, M. V. Bejanian, V. N. Smirnov, V. V. Filimonov, O. M. Zalite, S. Y. Venyaminov, *Eur. J. Biochem.* **1981**, *119*, 619.
- [20] Y. Liu, L. Blanchfield, V. P.-Y. Ma, R. Andargachew, K. Galior, Z. Liu, B. Evavold, K. Salaita, *Proc. Natl. Acad. Sci. USA* **2016**, *113*, 201600163.
- [21] L. Yu, Y. Hou, W. Xie, J. L. Cuellar-Camacho, Q. Wei, R. Haag, *Adv. Mater.* **2020**, *32*, 2006986.
- [22] L. Yu, Y. Hou, W. Xie, J. L. C. Camacho, C. Cheng, A. Holle, J. Young, B. Trappmann, W. Zhao, M. F. Melzig, *Adv. Mater.* **2020**, *32*, 2002566.
- [23] K. H. Vining, D. J. Mooney, *Nat. Rev. Mol. Cell Biol.* **2017**, *18*, 728.
- [24] N. Kim, E. Kim, H. Kim, M. R. Thomas, A. Najer, M. M. Stevens, *Adv. Mater.* **2021**, *33*, 2007738.
- [25] W. Baek, M. S. Bootharaju, K. M. Walsh, S. Lee, D. R. Gamelin, T. Hyeon, *Nat. Mater.* **2021**, *20*, 650.
- [26] W. Jiang, Z.-b. Qu, P. Kumar, D. Vecchio, Y. Wang, Y. Ma, J. H. Bahng, K. Bernardino, W. R. Gomes, F. M. Colombari, A. Lozada-Blanco, M. Veksler, E. Marino, A. Simon, C. Murray, S. R. Muniz, A. F. d. Moura, N. A. Kotov, *Science* **2020**, *368*, 642.
- [27] A. Bédier, F. Bonini, C. A. Verheyen, M. Genta, M. Martins, J. Brefie-Guth, J. Tratwal, A. Filippova, P. Burch, O. Naveiras, *Adv. Mater.* **2021**, *33*, 2102350.
- [28] Y. Zou, B. Huang, L. Cao, Y. Deng, J. Su, *Adv. Mater.* **2021**, *33*, 2005215.
- [29] M. Ryma, T. Tylek, J. Liebscher, C. Blum, R. Fernandez, C. Böhm, W. Kastenmüller, G. Gasteiger, J. Groll, *Adv. Mater.* **2021**, *33*, 2101228.
- [30] S. Li, X. Guo, R. Gao, M. Sun, L. Xu, C. Xu, H. Kuang, *Adv. Mater.* **2021**, *33*, 2005424.

- [31] S. Vermeulen, F. Honig, A. Vasilevich, N. Roumans, M. Romero, A. Dede Eren, U. Tuvshindorj, M. Alexander, A. Carlier, P. Williams, *Adv. Mater.* **2021**, *33*, 2102084.
- [32] T. T. Lee, J. R. García, J. I. Paez, A. Singh, E. A. Phelps, S. Weis, Z. Shafiq, A. Shekaran, A. Del Campo, A. J. García, *Nat. Mater.* **2015**, *14*, 352.
- [33] J. Han, Y. S. Kim, M. Y. Lim, H. Y. Kim, S. Kong, M. Kang, Y. W. Choo, J. H. Jun, S. Ryu, H. Y. Jeong, J. Park, G. J. Jeong, J. C. Lee, G. H. Eom, Y. Ahn, B. S. Kim, *ACS Nano* **2018**, *12*, 1959.
- [34] S. Zandi, S. Nakao, K. H. Chun, P. Fiorina, D. W. Sun, R. Arita, M. Zhao, E. Kim, O. Schueller, S. Campbell, M. Taher, M. I. Melhorn, A. Schering, F. Gatti, S. Tezza, F. Xie, A. Vergani, S. Yoshida, K. Ishikawa, M. Yamaguchi, F. Sasaki, R. Schmidt-Ullrich, Y. Hata, H. Enaida, M. Yuzawa, T. Yokomizo, Y. B. Kim, P. Sweetnam, T. Ishibashi, A. Hafezi-Moghadam, *Cell Rep.* **2015**, *10*, 1173.
- [35] F. Y. McWhorter, T. Wang, P. Nguyen, T. Chung, W. F. Liu, *Proc. Natl. Acad. Sci. USA* **2013**, *110*, 17253.
- [36] T. D. Zaveri, J. S. Lewis, N. V. Dolgova, M. J. Clare-Salzler, B. G. Keselowsky, *Biomaterials* **2014**, *35*, 3504.
- [37] H. Wang, D. J. Mooney, *Nat. Mater.* **2018**, *17*, 761.
- [38] K. Sadtler, A. Singh, M. T. Wolf, X. Wang, D. M. Pardoll, J. H. Elisseeff, *Nat. Rev. Mater.* **2016**, *1*, 16040.
- [39] W. Li, Z. Q. Yan, J. S. Ren, X. G. Qu, *Chem. Soc. Rev.* **2018**, *47*, 8639.
- [40] E. A. Cavalcanti-Adam, *Biophys. J.* **2007**, *92*, 2964.
- [41] J. A. Deeg, I. Louban, D. Aydin, C. Selhuber-Unkel, H. Kessler, J. P. Spatz, *Nano Lett.* **2011**, *11*, 1469.
- [42] J. H. Huang, S. V. Grater, F. Corbellin, S. Rinck, E. Bock, R. Kemkemer, H. Kessler, J. D. Ding, J. P. Spatz, *Nano Lett.* **2009**, *9*, 1111.
- [43] C. S. Chen, M. Mrksich, S. Huang, G. M. Whitesides, D. E. Ingber, *Science* **1997**, *276*, 1425.
- [44] L. Y. Koo, D. J. Irvine, A. M. Mayes, D. A. Lauffenburger, L. G. Griffith, *J. Cell Sci.* **2002**, *115*, 1423.
- [45] M. Schvartzman, M. Palma, J. Sable, J. Abramson, X. A. Hu, M. P. Sheetz, S. J. Wind, *Nano Lett.* **2011**, *11*, 1306.
- [46] J. Huang, S. V. Grater, F. Corbellini, S. Rinck, E. Bock, R. Kemkemer, H. Kessler, J. Ding, J. P. Spatz, *Nano Lett.* **2009**, *9*, 1111.
- [47] R. Changede, H. G. Cai, S. J. Wind, M. P. Sheetz, *Nat. Mater.* **2019**, *18*, 1366.
- [48] A. M. Rosales, K. S. Anseth, *Nat. Rev. Mater.* **2016**, *1*, 15012.
- [49] W. Li, Z. Yan, J. Ren, X. Qu, *Chem. Soc. Rev.* **2018**, *47*, 8639.
- [50] Y. Kim, H. Choi, J. E. Shin, G. Bae, R. Thangam, H. Kang, *View* **2020**, *7*, 20200029.
- [51] B. S. Gomes, B. Simões, P. M. Mendes, *Nat. Rev. Chem.* **2018**, *2*, 0120.
- [52] J.-U. Lee, W. Shin, Y. Lim, J. Kim, W. R. Kim, H. Kim, J.-H. Lee, J. Cheon, *Nat. Mater.* **2021**, *20*, 1029.
- [53] L. Zwi-Dantsis, B. Wang, C. Marijon, S. Zonetti, A. Ferrini, L. Massi, D. J. Stuckey, C. M. Terracciano, M. M. Stevens, *Adv. Mater.* **2020**, *32*, 1904598.
- [54] S. Min, M. J. Ko, H. J. Jung, W. Kim, S. B. Han, Y. Kim, G. Bae, S. Lee, R. Thangam, H. Choi, N. Li, J. E. Shin, Y. S. Jeon, H. S. Park, Y. J. Kim, U. K. Sukumar, J. J. Song, S. K. Park, S. H. Yu, Y. C. Kang, K. B. Lee, Q. Wei, D. H. Kim, S. M. Han, R. Paulmurugan, Y. K. Kim, H. Kang, *Adv. Mater.* **2021**, *33*, 2008353.
- [55] S. Min, Y. S. Jeon, H. J. Jung, C. Khatua, N. Li, G. Bae, H. Choi, H. Hong, J. E. Shin, M. J. Ko, H. S. Ko, I. Jun, H. E. Fu, S. H. Kim, R. Thangam, J. J. Song, V. P. Dravid, Y. K. Kim, H. Kang, *Adv. Mater.* **2020**, *32*, 2004300.
- [56] H. Hong, S. Min, S. Koo, Y. Lee, J. Yoon, W. Y. Jang, N. Kang, R. Thangam, H. Choi, H. J. Jung, S.-B. Han, Q. Wei, S.-H. Yu, D.-H. Kim, R. Paulmurugan, W. K. Jeong, K.-B. Lee, T. Hyeon, D. Kim, H. Kang, *Adv. Mater.* **2022**, *34*, 2105460.
- [57] Z. Liu, O. L. Lanier, A. Chauhan, *Nanomaterials* **2020**, *10*, 2359.
- [58] M. Cohen, D. Joester, B. Geiger, L. Addadi, *ChemBioChem* **2004**, *5*, 1393.
- [59] F. Oesterhelt, M. Rief, H. E. Gaub, *New J. Phys.* **1999**, *1*, 6.
- [60] B. Trappmann, J. E. Gautrot, J. T. Connelly, D. G. T. Strange, Y. Li, M. L. Oyen, M. A. C. Stuart, H. Boehm, B. J. Li, V. Vogel, J. P. Spatz, F. M. Watt, W. T. S. Huck, *Nat. Mater.* **2012**, *11*, 642.
- [61] S. J. Attwood, E. Cortes, A. W. M. Haining, B. Robinson, D. Y. Li, J. Gautrot, A. D. Hernandez, *Sci. Rep.* **2016**, *6*, 34334.
- [62] K. Maier-Hauff, F. Ulrich, D. Nestler, H. Niehoff, P. Wust, B. Thiesen, H. Orawa, V. Budach, A. Jordan, *J. Neurooncol.* **2011**, *103*, 317.
- [63] M. Prothmann, F. von Knobelsdorff-Brenkenhoff, A. Topper, M. A. Dieringer, E. Shahid, A. Graessl, J. Rieger, D. Lysiak, C. Thalhammer, T. Huelnhagen, P. Kellman, T. Niendorf, J. Schulz-Menger, *PLoS One* **2016**, *11*, e0148066.